PHOTONICS Research

Numerical analysis of end-fire coupling of surface plasmon polaritons in a metal-insulator-metal waveguide using a simple photoplastic connector

Yevhenii M. Morozov,[1,2] Anatoliy S. Lapchuk,[2] Ming-Lei Fu,[1] Andriy A. Kryuchyn,[2] Hao-Ran Huang,[1] and Zi-Chun Le[1,*]

[1]College of Science, Zhejiang University of Technology, Hangzhou 310023, China
[2]Institute for Information Recording of NAS of Ukraine, Shpak Str. 2, Kiev 03113, Ukraine
*Corresponding author: lzc@zjut.edu.cn

Received 4 September 2017; revised 30 December 2017; accepted 2 January 2018; posted 3 January 2018 (Doc. ID 306279); published 9 February 2018

We propose a design for efficient end-fire coupling of surface plasmon polaritons in a metal-insulator-metal (MIM) waveguide with an optical fiber as part of a simple photoplastic connector. The design was analyzed and optimized using the three-dimensional finite-difference time-domain method. The calculated excitation efficiency coefficient of the waveguide is 83.7% (–0.77 dB) at a wavelength of 405 nm. This design enables simple connection of an optical fiber to a MIM waveguide and highly efficient local excitation of the waveguide. Moreover, the length of the metallic elements of the waveguide, and thus the dissipative losses, can be reduced. The proposed design may be useful in plasmonic-type waveguide applications such as near-field investigation of live cells and other objects with super-resolution.

OCIS codes: (060.1810) Buffers, couplers, routers, switches, and multiplexers; (180.4243) Near-field microscopy; (250.5403) Plasmonics.

https://doi.org/10.1364/PRJ.6.000149

1. INTRODUCTION

Plasmonic nanostructures enable light waveguiding beyond the diffraction limit, making them potentially useful for applications such as super-resolution imaging [1], optical communications [2], and ultrahigh-density data storage [3]. Devices based on the metal-insulator-metal (MIM) structure are among the most promising because of their ability to minimize the losses that occur during nanofocusing processes. This ability is attributed to the fact that this structure has no cutoff size; further, all the energy from the probe base can propagate to the probe aperture, and the aperture is not shielded by a metal screen. In addition, the probe can possess a large tapering angle (which leads to a small probe length) in accordance with a rapid decrease in mode wavelength with decreasing MIM waveguide height. However, devices that can support surface plasmon polaritons (SPPs) suffer from high ohmic losses in the constituent plasmonic materials (usually gold, silver, or aluminum) [4]. This reduces the propagation distance of highly confined SPPs and therefore limits the application of such devices.

Owing to the high dissipative losses, it is crucial to use an excitation configuration in which SPPs can be excited with high energy efficiency and the length of the metallic elements of the plasmonic devices can be reduced. A major concern here is the efficiency of the interface between conventional micrometer-size photonics and plasmonics with sizes of tens of nanometers. SPPs cannot be excited by a single freely propagating photon because of the momentum mismatch between freely propagating light and SPPs on the metal surface. There are other methods of SPP excitation, such as use of the Kretschmann and Otto geometries [5], end-fire coupling [6], vertical excitation [7], use of diffraction gratings [8,9], and excitation by a focused laser beam [10,11].

MIM waveguides such as the recently fabricated gap plasmon waveguide with a three-dimensional (3D) linear taper [12] can play a crucial role in future near-field investigation of the features of live cells and other objects with super-resolution, owing to their unique ability to image biological processes at the cell membrane, the site of many medically important events [13,14]. Nevertheless, excitation of the structure by direct laser irradiation requires complex and precise adjustment of the entire system. At the same time, the creation of a high-power Gaussian beam using a fiber-coupled 405-nm diode laser system [15,16] and fiber lasers [17,18] is a well-known and extensively investigated process. In this work, we propose a design for efficient end-fire coupling of SPPs in a MIM waveguide with an optical fiber as part of a photoplastic

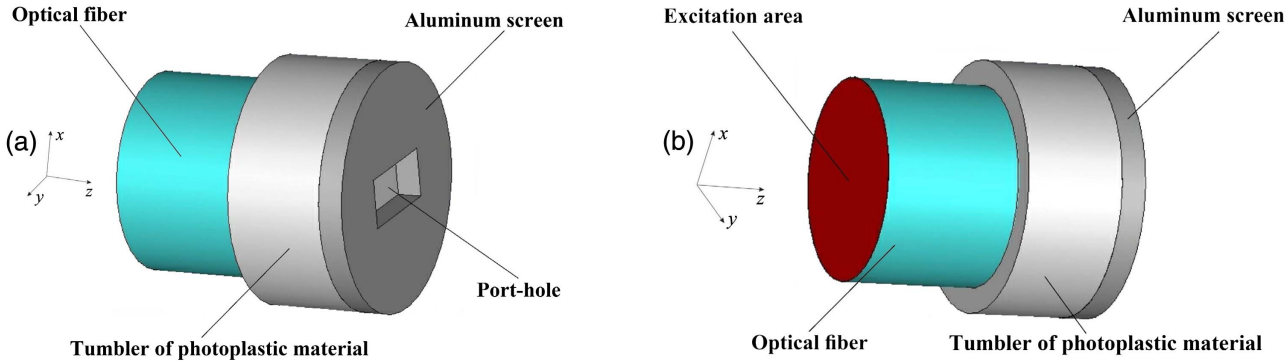

Fig. 1. Spatial geometry of the photoplastic connector: (a) view from the PH; (b) view from the excitation area.

connector. Fiber coupling of the laser beam to a near-field probe allows one to move only the MIM part of a scanning near-field optical microscope during object scanning, making it possible to significantly increase the speed and working area of the microscope. The main advantage of this design is that it enables simple connection of an optical fiber to a MIM waveguide and local excitation of the waveguides with high energy efficiency. In addition, use of the design allows one to reduce the length of the metallic elements of the MIM waveguide and, therefore, reduce the dissipative losses. The design was analyzed and optimized by the 3D finite-difference time-domain (FDTD) method [19] using light with a wavelength of 405 nm. Violet light was used in the simulation because it is very informative and widely employed for analysis of biological objects [20,21].

2. DESIGN OF THE PHOTOPLASTIC CONNECTOR

The spatial geometry of the connector is shown in Fig. 1. The connector consists of an aluminum screen and a hollow cylinder with a bottom (resembling a glass tumbler) made of photoplastic epoxy-type SU-8 material [22]. The optical fiber is inserted into the tumbler. A metal layer with a rectangular hole is deposited on the bottom of the tumbler. This port hole (PH) is used to connect the fiber to the MIM waveguide, and the aluminum screen is used to suppress background radiation. The structure was excited by the fundamental LP_{01} (HE_{11}) mode [23] of the optical fiber. The MIM waveguide is connected to the optical fiber via the PH. Figure 2 shows a schematic representation of the connector design with a legend.

The dimensions of the PH are also such that they allow only the fundamental TE_{10} mode to propagate in the PH. As considerable attention was paid to calculation of the fundamental symmetric plasmon quasi-TM_{00}-mode excitation efficiency in the MIM waveguide [24–26], the design of the waveguide was simplified to a regular line with transverse dimensions equal to the dimensions of the device base: $b = 200$ nm, $t = 50$ nm, $a = 500$ nm, and $L_5 = 1000$ nm. This rectangular base from Ref. [12] serves as the input coupler of a sub-100-nm-scale SPP focusing tip. The materials for the MIM waveguide were fused quartz (central layer) and aluminum (coatings).

3. NUMERICAL SIMULATION

A. Numerical Analysis Technique

The proposed design was numerically simulated by the 3D FDTD method [19]. The simulation was performed for light with a wavelength of 405 nm (frequency $f = 740$ THz). The Drude model was used to describe the interaction of the metals with electromagnetic radiation. The parameters of the employed materials were taken from Ref. [27]. The relative permittivity of aluminum is $-24 + i5$. We chose aluminum because of its low dissipative losses at 405 nm. The relative permittivity is 2.62 for the tumbler [28] and 2.16 for the optical

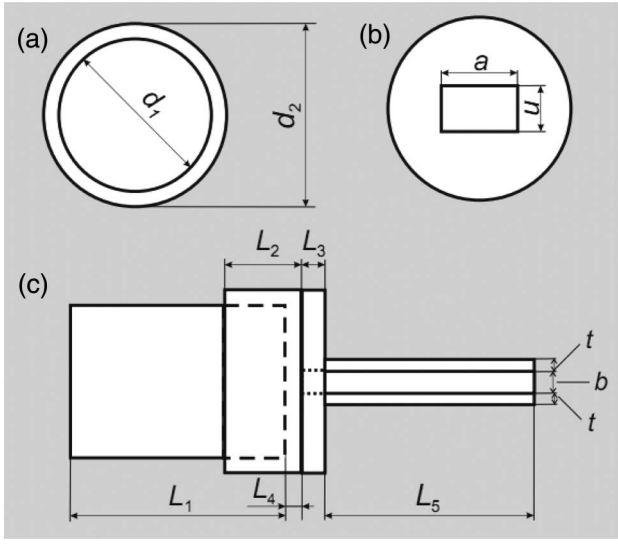

Fig. 2. Schematic representation of the connector design: (a) view from the excitation area, (b) view from the PH, and (c) longitudinal view. d_1 is a diameter of the optical fiber, and thus the inner diameter of the tumbler; d_2 is the external diameter of the tumbler, and thus the diameter of the Al screen; a and u are the width and height of the PH, respectively; L_1 is the length of the optical fiber; L_2 is the length of the tumbler; L_3 is the thickness of the Al screen; L_4 is the distance between the optical fiber and Al screen, that is, the thickness of the tumbler bottom; L_5 is the length of the MIM waveguide; b is the thickness of the MIM waveguide dielectric layer; t is the thickness of the MIM waveguide's metallic coatings.

fiber core and MIM waveguide fused quartz layer. The convergence of the results and mesh adaptation of the model were analyzed before the simulation. Note that end-fire coupling requires an optical fiber without cladding. In this case, the optical fiber can be considered as a circular dielectric waveguide. In the analysis, the fundamental propagating LP_{01} (HE_{11}) mode of a circular dielectric waveguide (Fig. 3) is considered.

An optical fiber with a reduced diameter of 1 μm was used to realize the single-mode regime as nearly as possible. The LP_{01} (HE_{11}) mode does not have a cutoff frequency and is commonly used in fiber optics.

Starting from the fundamental Maxwell's equations [29,30], the dispersion relation for the fundamental symmetric plasmon quasi-TM_{00} mode of the five-layer air–Al–SiO_2–Al–air structure (uniform and infinite along the y axis) was obtained in the form

$$-\frac{k_d}{\varepsilon_d}\mathrm{th}(k_d w) = \left\{\frac{k_m}{\varepsilon_m}\mathrm{th}[k_m(u-w)] + \frac{k_a}{\varepsilon_a}\right\} \cdot \left\{1 + \frac{k_a}{\varepsilon_a}\frac{\varepsilon_m}{k_m}\mathrm{th}[k_m(u-w)]\right\}^{-1}, \quad (1)$$

where $k_d^2 = \gamma^2 - \omega^2\varepsilon_d$, $k_m^2 = \gamma^2 - \omega^2\varepsilon_m$, and $k_a^2 = \gamma^2 - \omega^2\varepsilon_a$; γ is a complex propagation constant; ω is the angular frequency of the considered electromagnetic process; ε is the relative permittivity: $\varepsilon_d(SiO_2) = 2.16$, $\varepsilon_m(Al) = -24 + i5$, $\varepsilon_a(air) = 1$; $w = b/2$; and $u = b/2 + t$. For the quasi-TM_{00} mode, the electric field is expressed as $\bar{E} = \hat{x}E(x)\exp(j\gamma z)$ and is assumed to depend on the time τ as $\exp(-j\omega\tau)$. The electric field amplitude (E_x) profile of this mode is shown in Fig. 4.

A comparison of Figs. 3 and 4 reveals that the field structure of the LP_{01} (HE_{11}) mode is closest to the field of the fundamental symmetric plasmon mode of the MIM waveguide when the electric field polarization (transverse component) is orthogonal to the metal surface of the MIM waveguide [transverse magnetic (TM) mode]. Therefore, it should provide good coupling efficiency of the fiber mode to the MIM waveguide plasmon mode.

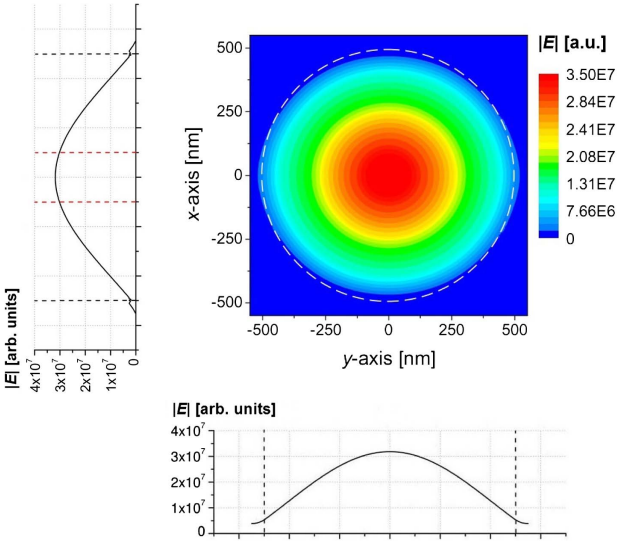

Fig. 3. Contour plot and profiles of the absolute value of the electric field of the fundamental propagation LP_{01} (HE_{11}) mode of a circular dielectric waveguide; white dashed circle corresponds to outer edge of the optical fiber core; red dashed lines correspond to the PH dimension along the x axis; a.u., arbitrary units.

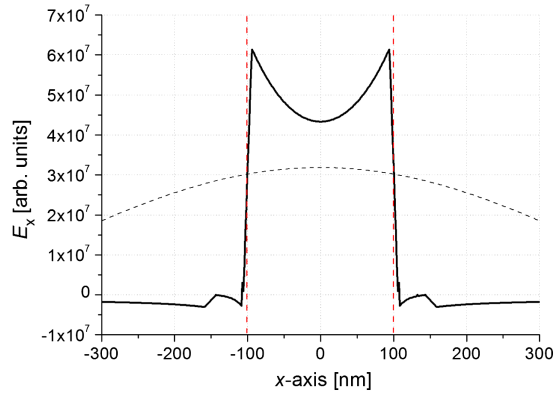

Fig. 4. Electric field amplitude (E_x) profile of the fundamental symmetric plasmon quasi-TM_{00} mode; $b = 200$ nm, $t = 50$ nm; red dashed lines correspond to the PH dimension along the x axis; black dashed line corresponds to the $|E|$ profile of the fundamental propagation LP_{01} (HE_{11}) mode of a circular dielectric waveguide along the x axis from Fig. 3.

The connector has a metal part that can cause significant dissipative losses. Therefore, the structure of the coupler should not have a high-Q-factor resonator, and all the parts of the connector should be well matched to each other to reduce the ohmic losses. To obtain the best match between the connector and the fiber, it is necessary to first analyze the parameters of the connector alone (without the MIM waveguide) before studying the MIM waveguide excitation efficiency.

This allows us to analyze the dependence on the connector parameters of the power coupling efficiency of an optical fiber directly with the connector and of the connector with the free-space plane waves. Here, the power transmission coefficient c_{eff_1} was considered. This coefficient is determined as the ratio of the radiant flux emitted by the PH and the radiant flux that falls on the PH. Therefore, c_{eff_1} indicates the ability of the connector to radiate light energy. It is determined by the following expression:

$$c_{eff\_1} = \frac{P}{P_0}, \quad (2)$$

where P_0 is the radiant flux through the circular control area S_0, and P is the radiant flux through a square control area S_{rad}. The area S_0 is located 10 nm in front of the Al screen and has a diameter of 600 nm. The area S_{rad} is located 10 nm behind the Al screen and has a size of 600 nm × 400 nm. P_0 was determined taking into account the wave reflection at the interface between the tumbler and the aluminum screen. To this end, first, the standing-wave ratio in the considered area was calculated, and then the power reflection coefficient $|R|^2$ was determined [31,32].

The MIM waveguide was then connected to the optical fiber via the PH. The coefficient of the MIM waveguide excitation efficiency, c_{eff_2}, is determined by Eq. (2) [32,33]. The measurement technique is described in detail in Ref. [32].

B. Results and Discussion

Figure 5 shows the dependence of $c_{\text{eff\_1}}$ and the power reflection coefficient $|R_1|^2$ at the control area S_0 on the Al screen thickness L_3. As shown in Fig. 5, $c_{\text{eff\_1}}$ and $|R_1|^2$ vary according to the harmonic law (sine) as the thickness of the aluminum screen, L_3, increases. Further, the functions $c_{\text{eff\_1}}(L_3)$ and $|R_1|^2(L_3)$ are phase-shifted relative to each other by approximately π. Although the fiber used in the simulation can support several waveguide propagation modes, the analyzed structure is highly symmetric, and higher fiber modes have little influence on the energy transmission in the structure.

All the other waveguides, which can be considered as parts of our structure, have only a few modes, which cannot be excited owing to structural symmetry [25]. Therefore, the analysis based on the single–mode approximation can give a good first-order approximation and will be used below for the energy transmission analysis.

We can consider the inhomogeneous area between the beginning of the tumbler and free space as an open resonator connected to the fiber on one end and to free space on the other side. Weak coupling efficiency from any side of the resonator would result in high reflection for any resonator length. If the coupling efficiency from both sides of the resonator is weak, the resonance of the reflection and transmission coefficients depends strongly on the resonator length. At resonance, the transmission and reflection coefficients exhibit a large narrow peak and deep dip at lengths far from the resonance length. However, the power transmission coefficient shown in Fig. 5 shows relatively large values for all resonator lengths. The harmonic variation and phase shift of π of the functions $c_{\text{eff\_1}}(L_3)$ and $|R_1|^2(L_3)$ can be attributed to the fact that in this case, the PH is a Fabry–Perot cavity with length L_3. As a result, as more energy is radiated from the resonator end, less energy is reflected back to the resonator. By varying the cavity length L_3, one can control the intensity of the reflected and transmitted electromagnetic waves. Here, the PH can be considered as a Fabry–Perot cavity with perfect electric conductors because the wavelength normalized by the height of the cavity, u/λ, is approximately 0.5, and the relative permittivity of aluminum is −24 [34]. In more detail, the PH can be represented as an unfilled two-plate line [35] with a characteristic impedance Z_0 and propagation constant β_1, which is open at the end. The line is loaded with an impedance Z_l approximately equal to the impedance of free space. The modulus of the complex reflection coefficient from the load can be written as

$$|\Gamma_l| = \left|\frac{Z_l - Z_0}{Z_l + Z_0}\right|. \tag{3}$$

From Eq. (3), it is obvious that the condition under which the complex reflection coefficient from the load Γ_l is equal to 0 is $Z_l - Z_0 = 0$, or $Z_l = Z_0$. The wavelength in the PH was determined using the standing wave pattern in the line. For the TE_{10} mode, the calculated characteristic impedance is $Z_0 = (u/a)(k/\beta_1)\eta_0 = 163.1\,\Omega$, where k is the free-space wavenumber, and $\eta_0 = (\mu_0/\varepsilon_0)^{1/2} \approx 377\,\Omega$. The modulus of Γ_l calculated by Eq. (3) is 0.4. In summary, at the control area S_0, the electromagnetic field can be represented as a superposition of one incident and two reflected waves. The first reflected wave was reflected at the tumbler/Al screen interface, and the second was reflected at the Al screen/free space interface (at the PH end). Therefore, the phase of the second reflected wave at S_0 changes depending on the thickness of the aluminum screen, L_3. This leads to a change in the total electromagnetic field at that point and a corresponding change in the radiant flux P_0, which can be seen in Fig. 5. A criterion of our optimization is to find the Al thickness that corresponds to the highest power transmission coefficient $c_{\text{eff\_1}}$. The highest value of $c_{\text{eff\_1}}$ is 79.5% at $L_3 = 50$ nm in the considered thickness range. Note that an Al screen thickness of 50 nm is sufficient to prevent light radiation through the screen (the skin depth of aluminum is approximately 25 nm at the wavelength of interest) and, therefore, to decrease the level of background radiation behind the Al screen.

Figure 6 shows the dependence of $c_{\text{eff\_1}}$ and $|R_1|^2$ on the distance L_4 between the optical fiber and Al screen, i.e., on the thickness of the photoplastic tumbler bottom (the thickness of the Al screen is 50 nm).

As shown in Fig. 6, the power transmission coefficient $c_{\text{eff\_1}}$ is approximately 79.5% at $L_3 = 50$ nm and $L_4 = 100$ nm. The data in Figs. 5 and 6 show only small peaks in the transmission coefficient at the resonance lengths and a relatively large transmission coefficient in the entire range of thicknesses

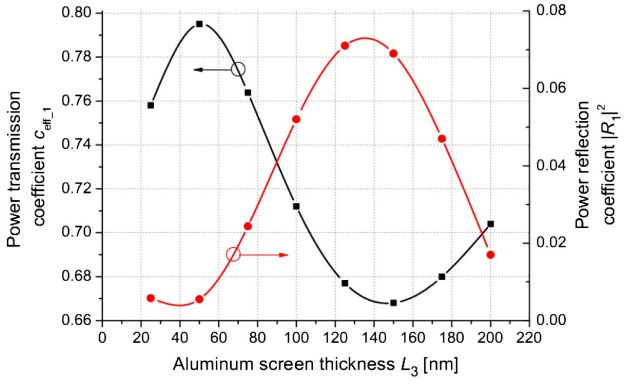

Fig. 5. Dependence of $c_{\text{eff\_1}}$ and power reflection coefficient $|R_1|^2$ on the Al screen thickness L_3; $d_1 = 1000$ nm, $d_2 = 1200$ nm, $L_1 = 500$ nm, $L_2 = 400$ nm, $L_4 = 100$ nm, $a = 500$ nm, $u = 200$ nm.

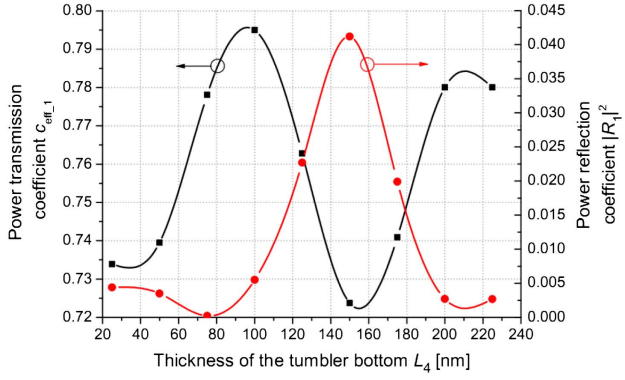

Fig. 6. Dependence of $c_{\text{eff\_1}}$ and $|R_1|^2$ on the tumbler bottom thickness L_4; $d_1 = 1000$ nm, $d_2 = 1200$ nm, $L_1 = 500$ nm, $L_2 = 400$ nm, $L_3 = 50$ nm, $a = 500$ nm, $u = 200$ nm.

of the simulated metal screen L_3 and the tumbler bottom L_4 (the smallest value is less than the largest one by 15.9% and 8.9% in Figs. 5 and 6, respectively). This fact confirms that the fundamental LP_{01} (HE_{11}) mode of the fiber has a large coupling efficiency to free-space plane waves, and therefore the thickness of the metal screen is not crucial to the coupling efficiency of this connector.

A cross-sectional view of the electric field and energy flux in the structure is shown in Fig. 7. The optical fiber obviously has a significant factor of the working mode coupling with plane waves in free space via the PH of the connector. In addition, local field enhancement appears at the external edges of the PH [36,37] [see Fig. 7(b)]. This enhancement makes it possible to locally excite the MIM waveguide with high efficiency.

In the next part of the simulation, the MIM waveguide was connected to the optical fiber via the PH of the connector. Note that the optimization of the connector parameters performed earlier gives only a qualitative estimate, because connecting the MIM waveguide to the optical fiber changes the conditions at the end of the PH. In this case, the load impedance Z_l is equal to the characteristic impedance of the MIM waveguide, $Z_{\mathrm{MIM}} = (b/a)(\beta_2/k\varepsilon)\eta_0 = 108.8\,\Omega$, where β_2 is the propagation constant of the MIM waveguide, and $\varepsilon = 2.16$. The wavelength of the MIM waveguide was determined using the standing wave pattern in the line. The modulus of Γ_l calculated by Eq. (3) is equal to 0.2 (it is half of that without the MIM waveguide). Therefore, in this case, the parameters of the connector are different from those obtained in the earlier calculation; however, the previously presented results give a good first-order approximation and may be fruitful for preliminary qualitative analysis of the connector parameters and understanding of connector operation.

Figure 8 outlines the dependence of the coefficient of the MIM excitation efficiency $c_{\mathrm{eff\_2}}$ calculated by Eq. (2) on the Al screen thickness L_3. The radiant flux P was determined taking into account the wave reflection at the end of the MIM waveguide. Because we calculated the fundamental symmetric quasi-TM_{00}-mode excitation efficiency in the MIM waveguide, we do not consider subsequent propagation of light along the MIM waveguide and the conditions at the MIM waveguide end (which generally do influence the field distribution in the connector).

The data in Fig. 8 are in good qualitative agreement with the results obtained without the MIM waveguide. The coefficient $c_{\mathrm{eff\_2}}$ is 83.7% (–0.77 dB) at $L_3 = 50$ nm. This finding confirms that the fundamental LP_{01} (HE_{11}) mode of the optical fiber core has high coupling efficiency to the fundamental symmetric quasi-TM_{00} mode of the MIM waveguide.

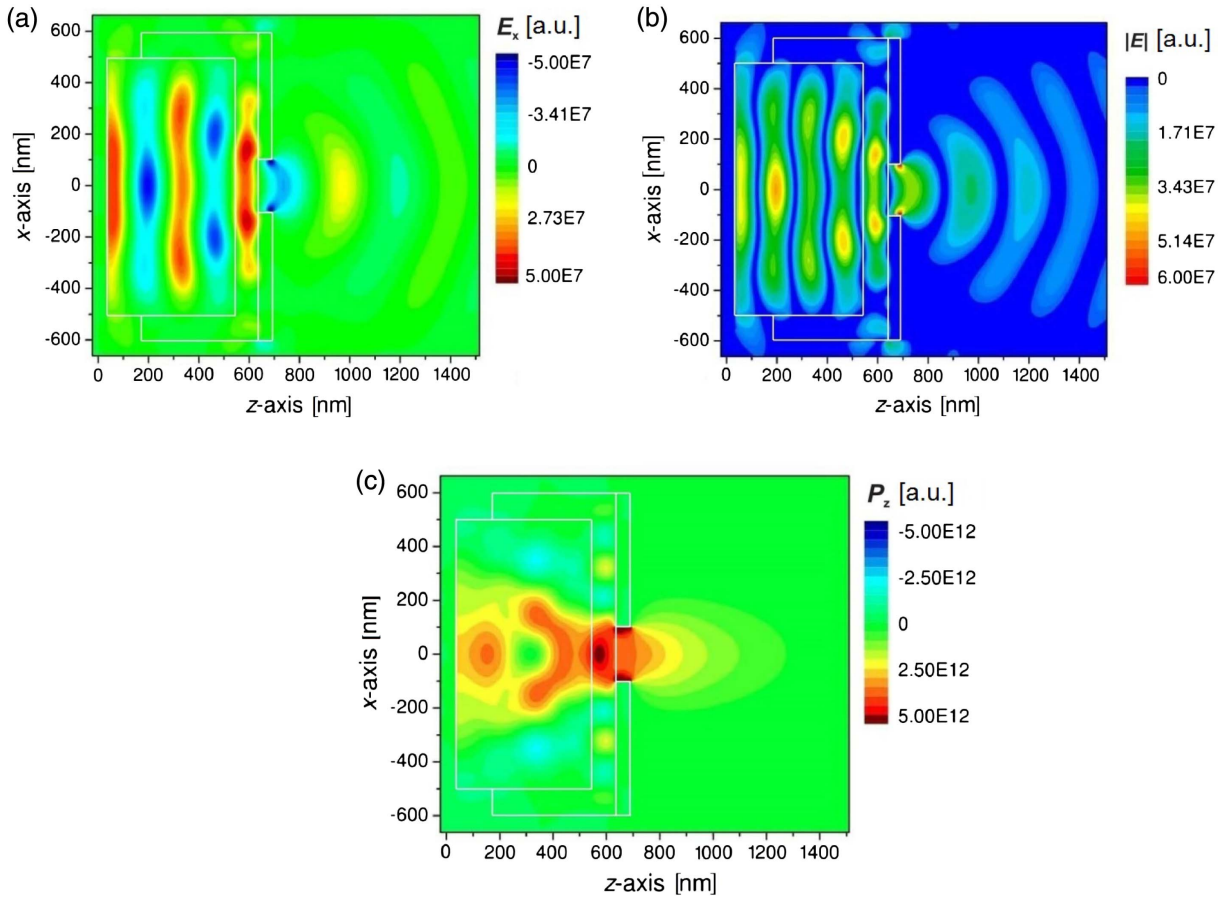

Fig. 7. Cross-sectional view of the electric field and energy flux in the structure: (a) x component of the electric field; (b) absolute value of the electric field; (c) z component of the Poynting vector. $d_1 = 1000$ nm, $d_2 = 1200$ nm, $L_1 = 500$ nm, $L_2 = 400$ nm, $L_3 = 50$ nm, $L_4 = 100$ nm, $a = 500$ nm, $u = 200$ nm; a.u., arbitrary units.

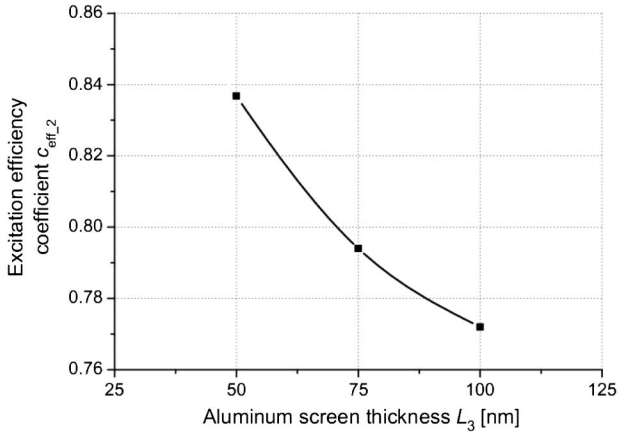

Fig. 8. Dependence of c_{eff_2} on the Al screen thickness L_3; $d_1 = 1000$ nm, $d_2 = 1200$ nm, $L_1 = 500$ nm, $L_2 = 400$ nm, $L_3 = 50$ nm, $L_4 = 100$ nm, $L_5 = 1000$ nm, $a = 500$ nm, $u = 200$ nm, $b = 200$ nm, $t = 50$ nm.

An aluminum screen thickness of less than 50 nm is undesirable because of field penetration through the screen.

A cross-sectional view of the electric field and energy flux in the structure with the MIM waveguide is shown in Fig. 9. In Figs. 9(a) and 9(b), the fundamental symmetric plasmon quasi-TM_{00} mode, which propagates along the MIM waveguide in the positive z direction, is clearly visible.

Note that when this photoplastic connector is used, the length of the waveguide base L_5 can be significantly reduced. This is because one can locally excite the MIM waveguide with high efficiency, and the aluminum screen reduces the background radiation to the device tip, so there is no need to strictly exclude the tip from the excitation area. In this case, the reduction in the length of the metallic elements leads to a reduction in the dissipative losses in the waveguide.

4. EXPERIMENTAL FEASIBILITY

Although our design is based on numerical analysis, the experimental process can be discussed on the basis of some experimental works [12,22]. The photoplastic connector is fabricated as follows: (1) an oxide layer is produced on the Si wafer by thermal oxidation; (2) after deposition of a sacrificial layer, the aluminum screen is created using vacuum evaporation; (3) photoplastic material is deposited on the Al screen using a spin-coating procedure [38]; (4) the photoplastic part is then exposed to ultraviolet (UV) radiation and developed to create a tumbler for the optical fiber; (5) the optical fiber is then inserted into the tumbler and fixed using UV glue; (6) the optical fiber in the connector is separated from the wafer; (7) at the end, a PH of appropriate size is created in the Al screen by focused ion beam milling. Note that the technological requirements for manufacturing the connector can be reduced because the excitation efficiency coefficient c_{eff_2} does not show

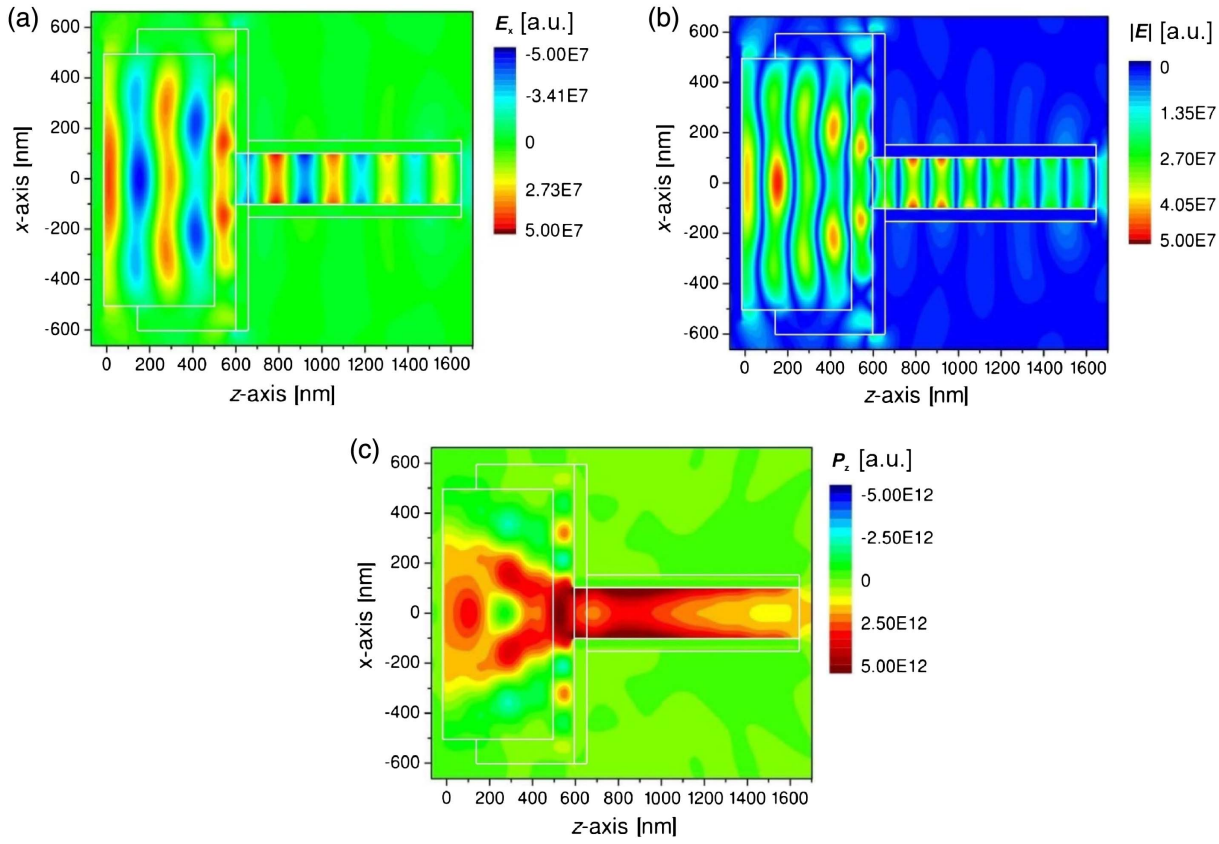

Fig. 9. Cross-sectional view of the electric field and energy flux in the structure with the MIM waveguide: (a) x component of the electric field; (b) absolute value of the electric field; (c) z component of the Poynting vector. $d_1 = 1000$ nm, $d_2 = 1200$ nm, $L_1 = 500$ nm, $L_2 = 400$ nm, $L_3 = 50$ nm, $L_4 = 100$ nm, $L_5 = 1000$ nm, $a = 500$ nm, $u = 200$ nm, $b = 200$ nm, $t = 50$ nm; a.u., arbitrary units.

a sharp resonant peak at certain values of the connector parameters. In Ref. [12], the process of MIM waveguide fabrication is described in detail.

Note that reducing the fiber core diameter may lead to LP_{01} mode energy leakage from the fiber core. To prevent this in our design, it is possible to produce a short fiber core tip with a reduced diameter using laser-heated pulling [39] and chemical etching [40] techniques.

Moreover, via the existing nanotechnologies, it is possible to create a substrate-based structure with free access to the base end face of the MIM waveguide. In addition, it has been shown [41] that the excitation efficiency is not very sensitive to the width of the incident beam and the position of its center on the MIM end face. In other words, in a real implementation, one can just connect an optical fiber to the MIM waveguide without needing to perfectly match the PH plane to the end face of the MIM waveguide.

5. CONCLUSIONS

Plasmonic nanostructures allow for light waveguiding beyond the diffraction limit, making them potentially useful for applications such as super-resolution imaging, optical communications, and ultrahigh-density data storage. Owing to the high dissipative losses in most plasmonic devices, it is crucial to excite SPPs with high energy efficiency. For this purpose, the design of efficient end-fire coupling of SPPs in a MIM waveguide with an optical fiber as part of a photoplastic connector was proposed. Detailed numerical analysis and optimization of the connector parameters were conducted. The calculated excitation efficiency coefficient of the MIM waveguide using the proposed photoplastic connector is 83.7% (−0.77 dB). Use of this design enables simple connection of an optical fiber to a MIM waveguide. In addition, the design makes it possible to reduce the length of the metallic elements of the MIM waveguide and thus decrease the dissipative losses. In summary, the proposed design of an optical fiber connection to MIM waveguides can be of practical importance in plasmonic-type waveguide applications such as near-field investigation of the features of live cells and other objects with super-resolution.

Funding. National Natural Science Foundation of China (NSFC) (61571399); "The Belt and Road" International Cooperation of Zhejiang Province, China (2015C04005).

REFERENCES

1. S. Kawata, Y. Inouye, and P. Verma, "Plasmonics for near-field nano-imaging and superlensing," Nat. Photonics **3**, 388–394 (2009).
2. J. Leuthold, C. Hoessbacher, S. Muehlbrandt, A. Melikyan, M. Kohl, C. Koos, W. Freude, V. Dolores-Calzadilla, M. Smit, I. Suarez, J. Martínez-Pastor, E. P. Fitrakis, and I. Tomkos, "Plasmonic communications: light on a wire," Opt. Photon. News **24**(5), 28–35 (2013).
3. M. Mansuripur, A. R. Zakharian, A. Lesuffleur, S.-H. Oh, R. J. Jones, N. C. Lindquist, H. Im, A. Kobyakov, and J. V. Moloney, "Plasmonic nano-structures for optical data storage," Opt. Express **17**, 14001–14014 (2009).
4. D. K. Gramotnev and S. I. Bozhevolnyi, "Plasmonics beyond the diffraction limit," Nat. Photonics **4**, 83–91 (2010).
5. A. V. Zayats and I. Smolyaninov, "Near-field photonics: surface plasmon polaritons and localized surface plasmons," J. Opt. A **5**, S16–S50 (2003).
6. C. S. Kim, I. Vurgaftman, R. A. Flynn, M. Kim, J. R. Lindle, W. W. Bewley, K. Bussmann, J. R. Meyer, and J. P. Long, "An integrated surface-plasmon source," Opt. Express **18**, 10609–10615 (2010).
7. E. Kinzel and X. Xu, "High efficiency excitation of plasmonic waveguides with vertically integrated resonant bowtie apertures," Opt. Express **18**, 10609–10615 (2010).
8. K. Li, F. Xiao, F. Lu, K. Alameh, and A. Xu, "Unidirectional coupling of surface plasmons with ultra-broadband and wide-angle efficiency: potential applications in sensing," New J. Phys. **15**, 113040 (2013).
9. P. A. Thomas, G. H. Auton, D. Kundys, A. N. Grigorenko, and V. G. Kravets, "Strong coupling of diffraction coupled plasmons and optical waveguide modes in gold stripe-dielectric nanostructures at telecom wavelengths," Sci. Rep. **7**, 45196 (2017).
10. H. Kano, S. Mizuguchi, and S. Kawata, "Excitation of surface-plasmon polaritons by a focused laser beam," J. Opt. Soc. Am. B **15**, 1381–1386 (1998).
11. J. Renger, R. Quidant, N. van Hulst, S. Palomba, and L. Novotny, "Free-space excitation of propagating surface plasmon polaritons by nonlinear four-wave mixing," Phys. Rev. Lett. **103**, 266802 (2009).
12. H. Choo, M.-K. Kim, M. Staffaroni, T. J. Seok, J. Bokor, S. Cabrini, P. J. Schuck, M. C. Wu, and E. Yablonovitch, "Nanofocusing in a metal-insulator-metal gap plasmon waveguide with a three-dimensional linear taper," Nat. Photonics **6**, 838–844 (2012).
13. D. M. Czajkowsky, J. Sun, and Z. Shao, "Illuminated up close: near-field optical microscopy of cell surfaces," Nanomed-Nanotechnol. **11**, 119–125 (2014).
14. H. A. Huckabay, K. P. Armendariz, W. H. Newhart, S. M. Wildgen, and R. C. Dunn, "Near-field scanning optical microscopy for high-resolution membrane studies," Methods Mol. Biol. **950**, 373–394 (2013).
15. C. P. Gonschior, K.-F. Klein, D. Heyse, S. Baumann, T. Sun, and K. T. V. Grattan, "High power 405 nm diode laser fiber-coupled single-mode system with high long-term stability," Proc. SPIE **8605**, 86050O (2013).
16. C. P. Gonschior, K.-F. Klein, M. Menzel, T. Sun, and K. T. V. Grattan, "Investigation of single-mode fiber degradation by 405-nm continuous-wave laser light," Opt. Eng. **53**, 122512 (2014).
17. W. Shi, Q. Fang, X. Zhu, R. A. Norwood, and N. Peyghambarian, "Fiber lasers and their applications," Appl. Opt. **53**, 6554–6568 (2014).
18. J. Xu, L. Huang, M. Jiang, J. Ye, P. Ma, J. Leng, J. Wu, H. Zhang, and P. Zhou, "Near-diffraction-limited linearly polarized narrow-linewidth random fiber laser with record kilowatt output," Photon. Res. **5**, 350–354 (2017).
19. A. Taflove, *Computational Electrodynamics: The Finite-Difference Time-Domain Method*, 3rd ed. (Artech House, 2005).
20. G. Patterson, M. Davidson, S. Manley, and J. Lippincott-Schwartz, "Superresolution imaging using single-molecule localization," Annu. Rev. Chem. **61**, 345–367 (2010).
21. A. Carpio, T. G. Dimiduk, M. L. Rapún, and V. Selgas, "Noninvasive imaging of three-dimensional micro and nanostructures by topological methods," SIAM J. Imaging Sci. **9**, 1324–1354 (2016).
22. G. Genolet, J. Brugger, M. Despont, U. Drechsler, P. Vettiger, N. F. de Rooij, and D. Anselmetti, "Soft, entirely photoplastic probes for scanning force microscopy," Rev. Sci. Instrum. **70**, 2398–2401 (1999).
23. J.-R. Qian and W.-P. Huang, "LP modes and ideal modes on optical fibers," J. Lightwave Technol. **4**, 626–630 (1986).
24. J. Zhu, W. Xu, Z. Xu, D. Fu, S. Song, and D. Wei, "Surface plasmon polariton mode in the metal-insulator-metal waveguide," Optik **134**, 187–193 (2017).
25. A. S. Lapchuk, D. Shin, H.-S. Jeong, C. S. Kyong, and D.-I. Shin, "Mode propagation in optical nanowaveguides with dielectric cores and surrounding metal layers," Appl. Opt. **44**, 7522–7531 (2005).
26. P. Ginzburg, D. Arbel, and M. Orenstein, "Gap plasmon polariton structure for very efficient microscale-to-nanoscale interfacing," Opt. Lett. **31**, 3288–3290 (2006).
27. E. D. Palik, *Handbook of Optical Constants of Solids* (Academic, 1985).
28. O. P. Parida and N. Bhat, "Characterization of optical properties of SU-8 and fabrication of optical components," in *Proceedings of the International Conference on Optics and Photonics*, Chandigarh, India, 30 October–1 November, 2009.

29. K. Y. Kim, ed., *Plasmonics–Principles and Applications*, 1st ed. (InTech, 2012).
30. S. H. Talisa, "Application of Davidenko's method to the solution of dispersion relations in lossy waveguiding system," IEEE Trans. Microwave Theory Tech. **33**, 967–971 (1985).
31. K. Kurokawa, "Power waves and the scattering matrix," IEEE Trans. Microwave Theory Tech. **13**, 194–202 (1965).
32. Y. M. Morozov and A. S. Lapchuk, "Signal of microstrip scanning near-field optical microscope in far- and near-field zones," Appl. Opt. **55**, 3468–3477 (2016).
33. L. Yu, L. Liu, Z. Zhou, and X. Wang, "High efficiency binary blazed grating coupler for perfectly-vertical and near-vertical coupling in chip level optical interconnections," Opt. Commun. **355**, 161–166 (2015).
34. R. Gordon, "Light in a subwavelength slit in a metal: propagation and reflection," Phys. Rev. B **73**, 153405 (2006).
35. D. M. Pozar, *Microwave Engineering*, 4th ed. (Wiley, 2012).
36. A. S. Lapchuk, S. A. Shylo, and I. P. Nevirkovets, "Local plasmon resonance at metal wedge," J. Opt. Soc. Am. A **25**, 1535–1540 (2008).
37. M. R. Disfani, M. S. Abrishamian, and P. Berini, "Electromagnetic fields near plasmonic wedges," Opt. Lett. **37**, 1667–1669 (2012).
38. H. Lorenz, M. Despont, N. Fahrni, J. Brugger, P. Vettiger, and P. Renaud, "High-aspect-ratio, ultrathick, negative-tone near-UV photoresist and its applications for MEMS," Sens. Actuators A **64**, 33–39 (1998).
39. G. A. Valaskovic, M. Holton, and G. H. Morrison, "Parameter control, characterization, and optimization in the fabrication of optical fiber near-field probes," Appl. Opt. **34**, 1215–1228 (1995).
40. J. Luo, Y. Fan, H. Zhou, W. Gu, and W. Xu, "Fabrication of different fine fiber tips for near field scanning optical microscopy by a simple chemical etching technique," Chin. Opt. Lett. **5**, 232–234 (2007).
41. G. I. Stegeman, R. F. Wallis, and A. A. Maradudin, "Excitation of surface polaritons by end-fire coupling," Opt. Lett. **8**, 386–388 (1983).